2019

Sandwich-structured, damage-resistant TiN/graded TiSiN/TiSiN film

Shuang Peng

Jiang Xu

Paul Munroe

Zonghan Xie
Edith Cowan University, z.xie@ecu.edu.au

10.1016/j.rinp.2018.12.019 Peng, S., Xu, J., Munroe, P., & Xie, Z. (2018). Sandwich-structured, damage-resistant TiN/graded TiSiN/TiSiN film. *Results in Physics, 12*, 543-554.
Available here.

Results in Physics 12 (2019) 543–554

Contents lists available at ScienceDirect

Results in Physics

journal homepage: www.elsevier.com/locate/rinp

Sandwich-structured, damage-resistant TiN/graded TiSiN/TiSiN film

Shuang Peng[a], Jiang Xu[a,*], Paul Munroe[b], Zonghan Xie[c,d]

[a] Department of Material Science and Engineering, Nanjing University of Aeronautics and Astronautics, 29 Yudao Street, Nanjing 210016, PR China
[b] School of Materials Science and Engineering, University of New South Wales, Sydney, NSW 2052, Australia
[c] School of Mechanical Engineering, University of Adelaide, SA 5005, Australia
[d] School of Engineering, Edith Cowan University, WA 6027, Australia

ARTICLE INFO

Keywords:
TiSiN graded interlayer
Deformation mechanism
Nanoindentation
Finite element method

ABSTRACT

The development of hard, multi-layer coatings is an effective strategy to enhance the wear resistance of cutting tools and so extend their service life. In the present study, a sandwich structured TiN/g-TiSiN/TiSiN film (where a graded (g-) TiSiN layer with an increasing Si content from 0 to 10 at% was inserted as a transitional layer between the TiN layer and the TiSiN layer with a fixed silicon content of 10 at%) was prepared on to a M42 tool steel substrate. Its mechanical properties were compared to both a dual-layered TiN/g-TiSiN film and a monolithic TiN film. Nanoindentation testing, assisted by focused-ion-beam (FIB) microscopy, was employed to evaluate contact-induced deformation and the mode of fracture of these films. Indented regions created on samples by a 5 μm radius indenter were examined by transmission electron microscopy (TEM). Finite element analysis was used to model the stress distributions within these films and predict the regions where crack initiation and growth may occur. The deformation of the monolithic TiN film was found to be predominantly accommodated by shear sliding along columnar grain boundaries, leading to a lower resistance to deformation. For the bilayer TiN/g-TiSiN film, the g-TiSiN layer hindered the propagation of columnar cracks, however, this bilayer film exhibited a stress concentration together with radial cracks at the bottom of the film. Compared with the former two films, the sandwich-structured film that contained the graded TiSiN interlayer exhibited the highest resistance to contact damage. This is because the graded TiSiN interlayer altered the stress distribution in the film and lowered the overall stress concentration level.

Introduction

Owing to its high hardness, good adhesion, chemical stability and low friction coefficient, titanium nitride (TiN) is an attractive candidate material to prolong the service lifetime and enhance the performance of various cutting tools [1–5]. Nevertheless, TiN thin films cannot satisfy the ever-increasing demand for the performance of cutting tools used in hostile conditions. For example, high-speed cutting is necessary for improved processing efficiencies and machining cost reduction, but the resultant high temperature generated at the contact area between cutting tool and workpiece and the intense friction that results can readily lead to failure of the TiN film, due to its poor oxidation resistance and insufficient hardness [6–9]. Therefore, much effort has been devoted to addressing these problems through tailoring the composition and structure of coatings based on substitutional alloying [10] or multilayer architecture methods [11].

The incorporation of Si, forming a nanocomposite (nc) structure consisting of nc-TiN embedded in amorphous a-Si_3N_4 matrix [12–14], leads to significant increases in both hardness and oxidation resistance. TiSiN nanocomposite films are reported to achieve extremely high hardness values greater than 40 GPa, when the addition of Si is about ~7 at% [15,16]. Prilliman et al. [17] suggested that such a notable increase in hardness resulted from a combined action of only elastic deformation occurring within TiN nanocrystals with diameters of only a few nanometers, while the amorphous a-Si_3N_4 boundary layers suppress grain boundary sliding. Further, the addition of Si is beneficial to the oxidation resistance of TiN, because the SiO_2 formed on the surfaces of the material has a lower oxygen diffusion rate than TiO_2 [18,19].

Despite these desirable properties, the main drawbacks of this nanocomposite coating are the high residual stress levels generated and its brittle nature. These lead to poor adhesion strength at the coating/substrate interface and deformation in a catastrophic fashion through the formation of lateral or radial cracks [20–22]. Inspired by natural composites, such as shells, bone and enamel, multilayered coatings that consist of two or more distinct layers of dissimilar materials arranged alternately, have been developed. Those multilayered coatings exhibit a

* Corresponding author.
E-mail address: xujiang73@nuaa.edu.cn (J. Xu).

https://doi.org/10.1016/j.rinp.2018.12.019
Received 29 November 2018; Accepted 4 December 2018
Available online 07 December 2018

higher resistance to crack propagation and high temperature oxidation, compared to monolithic coatings [23,24]. Furthermore, previous modelling studies have indicated that graded multilayer coatings, with a progressive increase in modulus from the coating/substrate interface to the coating outer surface, are able to avoid the generation of stress discontinuities at the interface coating/substrate and this then decreases the stress intensities both in the substrate and in the coating [25]. PalDey et al. [26] found that graded (Ti,Al)N coatings with a graded distribution of Al concentration exhibited much higher critical loads for coating adhesion than monolithic (Ti,Al)N coatings. This then demonstrated the potential to improve the properties of wear resistant coatings. Through both experimental work and computational simulation, Suresh et al. [27] also demonstrated that the glass-infiltrated alumina with controlled gradients in elastic modulus exhibited more resistant to frictional sliding contact damage than either monolithic alumina or glass, separately, or in an alumina–glass composite.

In this study, a sandwich structured TiN/g-TiSiN/TiSiN multi-layer film with a graded (g-) TiSiN interlayer was fabricated onto a M42 tool steel substrate using unbalanced magnetron sputtering. The deformation behavior of this multi-layered film was compared with both a dual-layered TiN/g-TiSiN film and a monolithic TiN film through both instrumented nanoindentation experiments and numerical simulations. To elucidate the influences of the multilayer architecture on the deformation mechanism of the sandwich-structured film, focused ion beam (FIB) cross-sectional morphologies of indentations, induced by a spherical-tipped conical indenter, were observed either directly or by transmission electron microscopy (TEM) examination. Finite element simulations were also used to investigate the effect of the film architectures on stress development of these films during nanoindentation.

Experimental procedure

Sample preparation

AISI M42 tool steel (hardened to HRC 65) was used as the substrate material in this study. The substrates were finely polished only on one side to an average surface roughness of 0.03 μm. The coatings were deposited using a UDP650 closed field unbalanced magnetron sputtering system with a four-target configuration (Teer Coatings Ltd., UK). Details of the deposition process have been described elsewhere [28]. There were four targets (three Ti and one Si) involved in the closed field unbalanced magnetron system, each was 380 mm × 170 mm in size, which was vertically aligned in the cylindrical PVD reactor. Prior to deposition, the background pressure of the sputtering system was reduced to less than 2.0 × 10–6 Torr, then Ar gas flow was admitted and controlled to maintain a working pressure of 1.3 × 10–3 Torr. In order to remove any oxide layer or contaminant on the surface, the substrates were ion etched using an Ar plasma at a bias voltage of −600 V for 30 min. During deposition, the substrate bias power was kept constant at −60 V, while the Ti target current was maintained at 8 A. The deposition temperature was fixed at 550 °C. The substrates were rotated at a speed of 10 rpm to promote coating homogeneity. A reactive N_2 gas flow was admitted continuously during the process for the growth of nitrides and the nitrogen concentration was automatically controlled via an optical emission monitoring (OEM) system. For better adhesion, a titanium wetting layer approximately 0.2 μm thickness was initially deposited on the substrate surfaces by applying a current of 8 A to the Ti targets for 10 min. Then, a TiN layer with the thickness of ~2 μm was deposited for the monolithic TiN film sample. A TiN layer, with a thickness of 0.4 μm, was deposited onto the other two specimens. Afterwards, the current of the Si target was increased linearly up to 2.5 A, so that a graded TiSiN layer was formed on the monolithic TiN layer and deposited onto the TiN/g-TiSiN sample and TiN/g-TiSiN/TiSiN sample with thicknesses of 1.6 μm and 0.6 μm respectively. For the final stage, the Si target current was maintained at 2.5 A and a TiSiN layer with the thickness of ~1 μm was deposited on the TiN/g-TiSiN/TiSiN sample, this layer contained a constant Si content of about 10 at %.

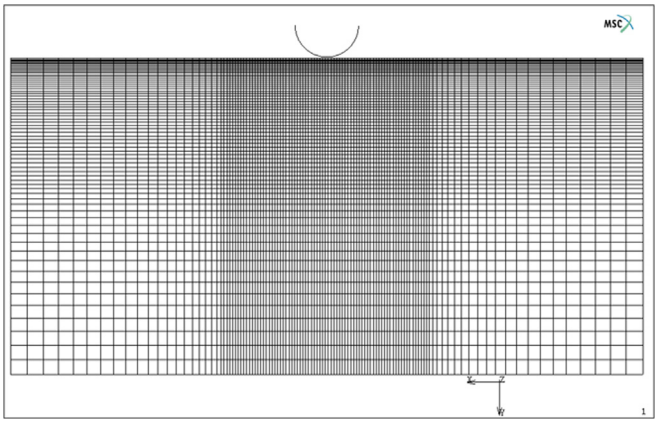

Fig. 1. Finite element model configurations for the simulation of indentation.

Nanoindentation

To introduce inelastic deformation and fracture damage in the coatings, an Ultra-Micro Indentation System (UMIS-2000, CSIRO, Sydney), equipped with a spherical-tipped conical indenter of 5 μm radius was employed. The spherical indenter tip was chosen as the stress field is more uniformly distributed under the indenter tip compared with sharper indenter types. For each specimen, maximum loads of 100 mN, 300 mN and 500 mN were applied. The contact force was initially set to 0.015 mN, and then increased in a square root progression, where there were a larger number of force increments at the beginning of loading compared to that nearer to the maximum load. Each loading and unloading procedure was performed in 50 steps with a 0.1 s dwell time following each increment and hold for 30 s at the peak load. To obtain more accurate data, 6 indentations were applied for the maximum load with 50 μm spacing between indents on each sample surface.

Microstructural characterization

A focused ion beam (FIB) microscope (FEI xP200) was used for milling and imaging microstructural cross-sections and also for transmission election microscopy (TEM) sample preparation. Details of these procedures have been given elsewhere [29]. Briefly, a protective layer of platinum (~1 μm thick) was initially deposited onto the coating surface in the vicinity of the indent, and then cross-sections of the indented region were milled by the ion beam, using beam currents of 2700 pA or 6600 pA for the initial cuts and then from 1000 pA down to 150 pA for final cleaning. Subsequently, the sample was tilted to 30°−45° for imaging, with minimal specimen damage, using a beam current of 11 pA or 70 pA. The images were obtained from ion-beam induced secondary electrons [30]. Further, TEM samples of both undeformed and deformed samples were characterized using a Philips CM 200 field emission gun TEM (FEGTEM) operating at 200 kV and VG 601 UX operating at 100 kV. Both bright field and dark field images were acquired to examine the cross-sectional microstructures of samples. Samples for TEM analysis were prepared using ex-situ lift out using a Fei Nova Nanolab FIB.

First-principles calculations

First-principles calculations was performed to explore the influence of Si additions on the mechanical properties of the TiSiN. The calculation based on density functional theory (DFT) was implemented with the Cambridge Sequential Total Energy Package (CASTEP) code using

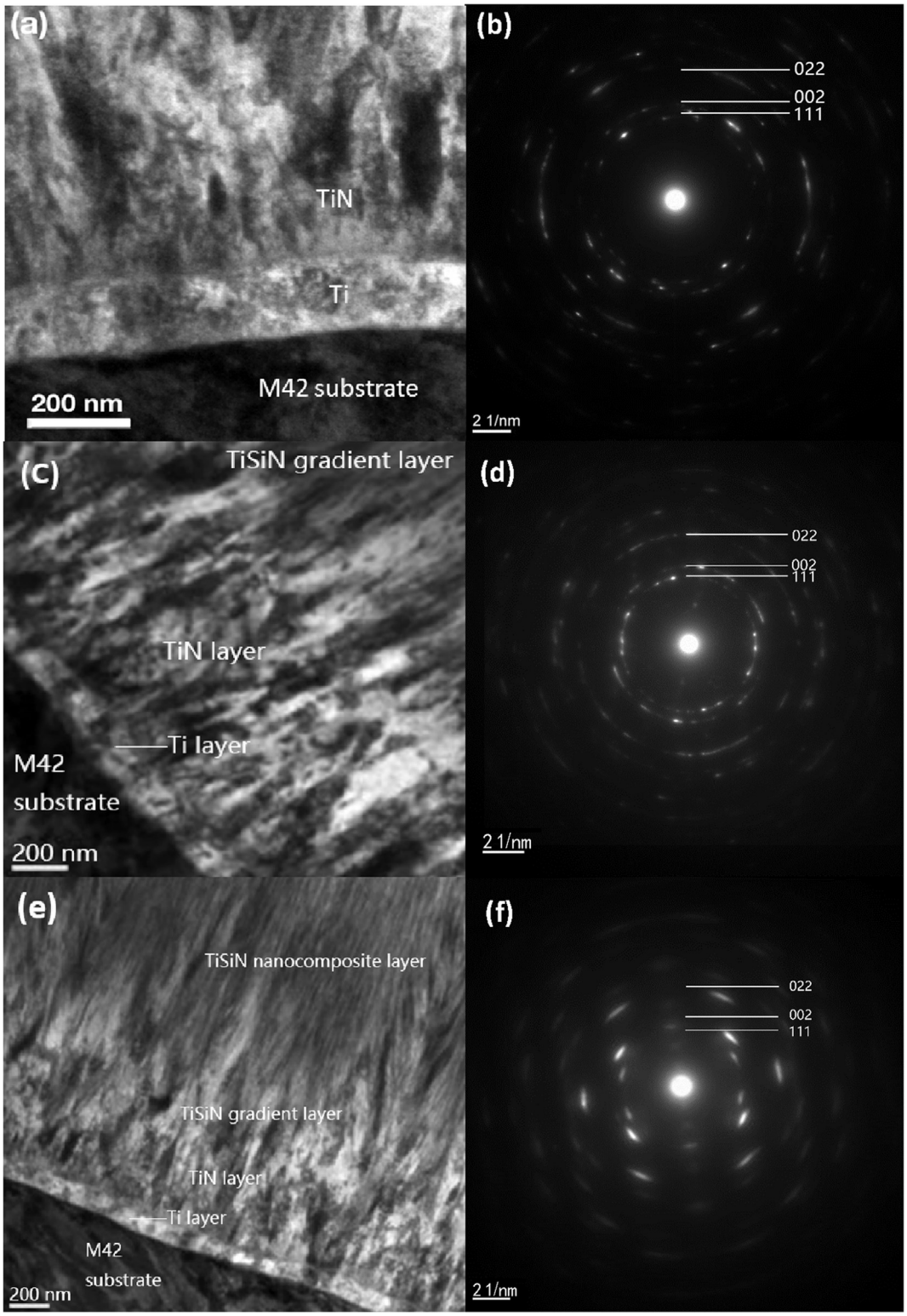

Fig. 2. Bright field TEM image of (a) the TiN film, (c) the TiN/g-TiSiN film and (e) the TiN/g-TiSiN/TiSiN film deposited on the M42 tool steel substrate and the corresponding SAD patterns obtained from (b) the TiN layer in the TiN film, (d) the TiSiN gradient layer in the TiN/g-TiSiN film and (f) the TiSiN nanocomposite layer in the TiN/g-TiSiN/TiSiN film.

the Perdew–Burke–Ernzerhof exchange–correlation in the framework of the generalized-gradient approximation (GGA)[31]. A supercell method was used to build the NaCl type structured TiSiN. 24 Ti atoms and 24 N atoms were contained in the $1 \times 2 \times 3$ supercell. The TiSiN with different Si concentration was construct by different amounts of Si atoms replacing Ti atoms. A cutoff energy of 350 eV and $3 \times 3 \times 2$ k-points mesh generated by the Monkhorst–Pack method [32] were used after convergence tests. The calculation of elastic moduli and Poisson's ratio of TiSiN were based on the Voight–Reuss–Hill approximation [33].

Table 1
Configuration of three coating systems modelled in this work.

Modelling sample	TiN layer (μm)	TiSiN gradient layer (μm)	TiSiN nanocomposite layer (μm)	Total thickness (μm)
a	2.0	–	–	2.0
b	1.0	1.0	–	2.0
c	0.4	0.6	1.0	2.0

Finite element simulation

In this simulation, a two-dimensional finite element model was employed to reduce computational time without compromising accuracy of the simulations. For all the simulations, it was assumed that the coating is perfectly adhered to the substrate and, further that there is frictionless contact between the coating and the indenter. It was further assumed that all the interfaces between the different layers were perfectly bonded. A static analysis was adopted on the assumption that the loading process was slow. The indenter and the substrate were identical for all three simulations. The indenter that was used had a spherical tip with a radius of 5 μm. The total scale of substrate and the film simulated was 50 μm in height and 100 μm in width. The substrate was divided into two sections as indicated in Fig. 1. The mesh is refined directly below the indenter for accuracy and gradually coarser closer to the edge. The boundary conditions of the left and right-hand side are set to restrain the nodal displacement in the x and z direction and the rotation of y-axis. The bottom is fixed in the y direction but was allowed to move in the other directions. Because the model dimensions are significantly larger than the coating thickness, any edge effects from the boundary constraints are negligible. Indenter movement was simulated as a downwards displacement according to the force–displacement curve of 500 mN, which is assumed to correspond to a maximum indentation load of 500 mN. The deformation of the substrate was modelled in an elastic–plastic manner.

Results and discussion

Microstructural analysis

Fig. 2 shows typical cross-sectional TEM bright-field images recorded from the monolithic TiN film, a dual-layered TiN/g-TiSiN film and the sandwich-structured TiN/g-TiSiN/TiSiN film. The selected area electron diffraction (SAED) patterns inset in each micrograph were obtained from the TiN layer in the TiN film (a), the TiSiN gradient layer in the TiN/g-TiSiN film (b) and the TiSiN out layer in the TiN/g-TiSiN/TiSiN film (c), respectively. The corresponding Miller indices (hkl) of each ring are labelled. The configurations of the three coating systems studied in this paper were listed in Table 1, which was used in the subsequent work for the finite element simulation.

The monolithic TiN film consists of columnar TiN grains, together with the Ti buffer layer, with a total film thickness of about 2.2 μm. The columnar grains extend across the TiN layer, with their long axis oriented in a direction perpendicular to the substrate surface.

The dual-layered TiN/g-TiSiN film, shown in Fig. 2(b), includes a TiSiN graded layer deposited on the TiN columnar structure layer that is about the same thickness as the monolithic TiN film. Although there was no distinct interface between the TiN layer and the graded TiSiN layer, the columnar structure became finer moving from the TiN layer to the TiSiN graded layer with an increasing concentration of Si incorporated into the film during the deposition process. A similar observation was also reported by Cairney et al. [34] for dual-layer TiN/TiAlN coatings.

According to the preparation of TiN/g-TiSiN/TiSiN film, a TiSiN nanocomposite layer was deposited on the TiSiN graded layer and harmonized the thickness with each layer to maintain the overall film thickness to be about 2.2 μm. Nevertheless, no clear interface was observed between the two layers nor any distinct change in the microstructure. The transition region of the TiN layer and the g-TiSiN layer was similar to the second film. Thus, the structure of the g-TiSiN layer was difficult to distinguish from the structure of the TiN/g-TiSiN/TiSiN film. In other words, the g-TiSiN layer played the role of the transition layer to avoid a sudden change of microstructure between the TiN layer and TiSiN layer. The same function was expected to be found on the mechanical properties of the TiN/g-TiSiN/TiSiN film.

The three brighter concentric Debye–Scherrer rings, which can be found in each SAED pattern, were consistent with the Bragg reflections for cubic TiN and corresponded to the (1 1 1), (2 0 0) and (2 2 0) planes from the inside outwards. No other phase was observed from the SAED patterns. Fine detail in the SAED pattern indicated changes between each layer. In the TiN layer, the measured lattice parameter was 0.43 ± 0.05 nm. This was slightly larger than the value of the g-TiSiN layer (0.42 ± 0.06 nm) and the TiSiN nanocomposite layer (0.41 ± 0.04 nm). The slight reduction in lattice parameter is likely due to the incorporation of Si atoms of smaller atomic radius, where Si replaces Ti in the TiN lattice [35,36].

The Si in the TiSiN layer existed both in the form of solid solution and the SiN_x phase according to a previous study [36,37]. The high content of Si in this layer may led to a thicker SiN_x interfacial phase and further result in the generation of the amorphous Si_3N_4 phase [38]. The arc-shaped diffraction reflections observed in the diffraction pattern from the TiSiN layer in Fig. 2c likely resulted from the presence of the SiN_x phase. As reported [36], the crystallite size of TiN grains was reduced with the increasing Si concentration. A smaller crystallite size and thus a more accurate analysis can result from arc-shaped diffraction reflections. In addition, the finer TiN grains, which presumably arose from the separation of a SiNx interfacial phase during the deposition process, may exhibit a wider distribution of orientations in the TiSiN nanocomposite layer.

The SAED pattern from the TiSiN graded layer shows Bragg reflections for TiN, but no reflections for the Si_3N_4 phase were observed. A larger number of diffraction reflections distributed in the corresponding diffraction rings suggested that the columnar grains were transformed into finer grains with a range of different crystal orientations as the Si content increased throughout the TiSiN layer. Different from the high-volume fraction of the Si_3N_4 amorphous phase in the TiSiN nanocomposite layer which obstructs the growth of the TiN grain, the low content of Si in the TiSiN graded layer affects the microstructure by increasing the nucleation rate of the TiN. The more Si doped, the greater the nucleation rate became and thus the finer the grain size presented [39,40].

In addition, at lower Si contents (less than 8 at%), attention has been focused on the SiN_x phase distributed around the TiN grain boundaries [38,41]. The crystallized SiN_x phase (< 0.7 nm in thickness) grows epitaxially on the TiN grains, which has been observed to hinder dislocation slip [37,42]. The extent of this interfacial area was increased through the incorporation of Si and this contributes to the strength of the g-TiSiN film.

Nanoindentation tests

Fig. 3 shows the force–displacement curves from the monolithic TiN film, the TiN/g-TiSiN film and the TiN/g-TiSiN/TiSiN film, subjected to nanoindentation to maximum loads of 100 mN (a), 300 mN (b) and

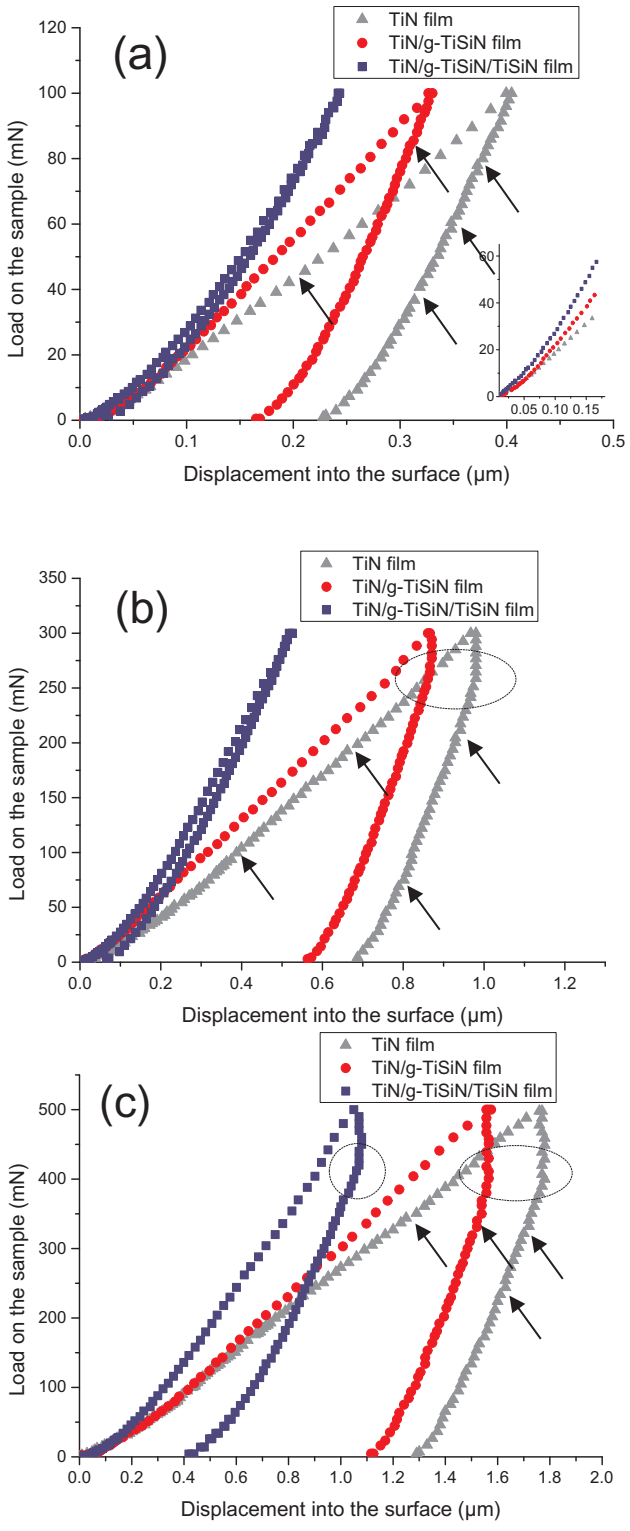

Fig. 3. Force-displacement curves for the three samples following nanoindentation, using the 5 μm radius indenter, up to a maximum load of 100 mN (a), 300 mN (b) and 500 mN (c).

500 mN (c), using a 5 μm radius spherical indenter.

At very low loads (0–20 mN) the maximum depth of penetration is less than the 10% thickness of the entire film according to the inset graph shown in Fig. 2a. The load–displacement curve mainly reflects the hardness of the films excluding the contribution from the substrate. It is obvious that the g-TiSiN layer increases the hardness of the TiN/g-TiSiN film relative to the TiN film. Further with the TiSiN layer deposited on the g-TiSiN layer, the TiN/g-TiSiN/TiSiN film exhibits the highest hardness in the initial stages of the indentation.

Under maximum loads of 100 mN, 300 mN and 500 mN, the load–displacement behavior of TiN/g-TiSiN/TiSiN film is mainly elastic and reversible and only a small amount of plastic deformation is detected. While the plastic deformation is clear in the TiN film and the TiN/g-TiSiN film, the sandwich structure film with the g-TiSiN interlayer still exhibits the highest hardness and protects the substrate from contact damage.

At the three different maximum loads shown in Fig. 3, there are indications of pop-in events (that is, sudden changes in indentation depth with a small increase in load) in all the three films. Examples are marked by the black arrows and dotted circles for each curve in Fig. 3. In brittle materials, pop-in events indicate a high energy release [43], which is normally associated with crack initiation and propagation [44,45] or delamination of the films [46]. The pop-ins observed here are divided into two categories.

Pop-ins marked by arrows represent minor events. They are of limited size in the load–displacement curve and some are difficult to discern. Further, they have only minor effects on the slope of the curve. For the TiN film, they appear on both of the load and unload curves. In the TiN/g-TiSiN film, they are only observed on the unloading curve and they are not detected at all for the TiN/g-TiSiN/TiSiN film. Based on the structure of these films, these small pop-in events are interpreted as the initiation of cracks or other minor failures in the film [47]. Thus, it can be suggested that the g-TiSiN layer refines the structure of TiN and hinders the initiation of cracks during the loading process in the TiN/g-TiSiN film and limits the formation of small cracks during the unloading process in the TiN/g-TiSiN/TiSiN film.

The other pop-ins marked by the dotted circles indicate more severe events. They are all observed in the unloading process and represented by changes in the slope of the load–displacement curve. Under a maximum load of 100 mN, no event is observed in the films. When the maximum load is increased to 300 mN, pop-ins appear both in the TiN film and TiN/g-TiSiN film. When the maximum load is 500 mN, pop-ins can be detected in all of the films. These severe pop-in events represent the propagation of the cracks in the films. Thus, it can be indicated that in the single g-TiSiN layer cracks propagate readily. However, when the TiSiN layer is added, the resistance to the propagation of the cracks can be significantly increased.

In summary, the TiN/g-TiSiN/TiSiN film exhibits not only shallower penetration depth at maximum load, but also the highest recovery rate (can be calculated by $1 - \frac{h_r}{h_{max}}$, where h_r is the residual indentation depth and h_{max} is the maximum penetration depth), which indicates that this film has the highest resistant to contact damage. Thus, the sandwich structure with the g-TiSiN interlayer greatly assists in hindering the initiation and propagation of cracks.

FIB cross-sectional images and surface morphology

Fig. 4 shows ion-induced secondary electron images of the outer surface topography for the three samples subjected to nanoindentation to a maximum load of 500 mN with a spherically-tipped indenter with a radius of 5 μm. The indentation diameters of the TiN film, the TiN/g-TiSiN film and the TiN/g-TiSiN/TiSiN film were 7.0 μm, 6.8 μm and 5.0 μm, respectively. The smaller the diameter of the indentation, the higher plastic deformation resistance of the film and hence higher the hardness. The radial cracks marked by the blue arrow were only observed for the TiN film. In addition, nest cracks, marked by the red arrow, were distributed near the edge of the indentation. Fewer cracks were observed in the TiN/g-TiSiN/TiSiN film, which indicated higher deformation resistance.

Fig. 5 shows FIB cross-sections of the three coatings following nanoindentation under a maximum load of 500 mN with a 5 μm spherical indenter. The thin dark layers between the film and the substrate

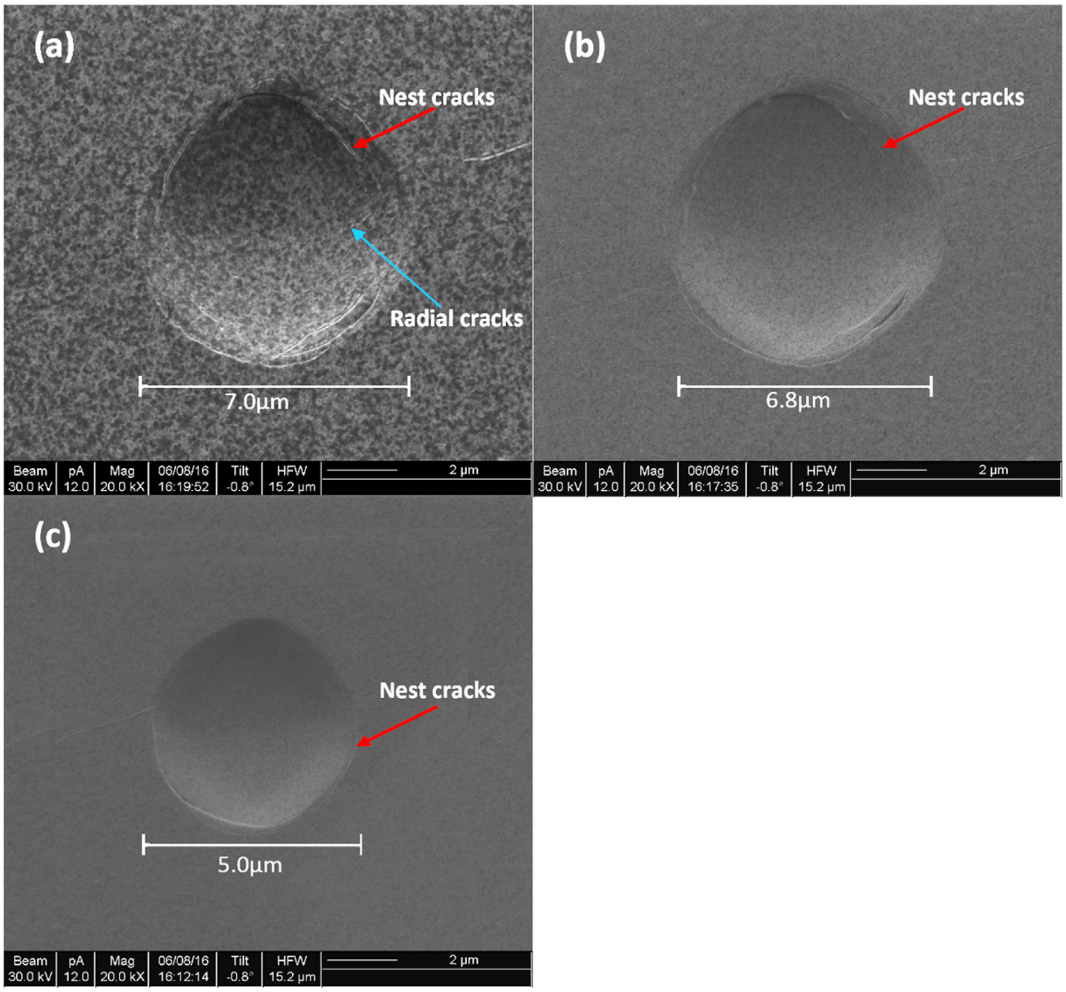

Fig. 4. FIB images of the top surface of the (a) the TiN film (b) the TiN/g-TiSiN film and (a) the TiN/g-TiSiN/TiSiN film.

represent the Ti wetting layer and no discernable delamination was observed in any of the three film/substrate systems, indicating that the Ti layer is effective as a wetting layer and acts to improve the adhesive strength of all three films. As shown in Fig. 5a and b, the TiN film and the TiN/g-TiSiN film are more heavily deformed, and the maximum penetration depth was measured to be 0.92 μm and 0.82 μm, respectively. In addition, the thickness of all the indented films is broadly uniform across the indented region, indicating that the coatings themselves do not undergo significant plastic flow during indentation [48]. Plastic deformation thus takes place in the substrate underneath the spherical indent, as marked by the pink arrow in Fig. 5a. The microstructure of the substrate underneath the impression exhibits elongated grains that indicate the plastic deformation of the steel. The depth of TiN/g-TiSiN/TiSiN film indentation was the lowest at 0.29 μm, and only a small amount of plastic deformation was observed in the substrate, indicating that TiN/g-TiSiN/TiSiN film has an enhanced capacity to resist deformation. A significant reduction in surface roughness was detected in the TiN film especially at the center of the indentation, relative to the periphery of the indentation. This shows that there is a compressive stress at the surface of the film under the indentation. The compressive stress at the surface of the film can restrain the growth of surface cracks [49,50].

A small number of radial cracks appeared in the TiN film near the center of the indent, as marked by blue arrows. While, no radial crack can be observed on the surface of the nanoindentation for both TiN/g-TiSiN and TiN/g-TiSiN/TiSiN films. The radial cracks visible on the surface of the indentation were identified to initiate at the coating/substrate interface [51] and are explained as the result of the tensile stresses at the bottom of the film [52]. Thus, under increasing indentation load, TiN film underwent bending and suffer increased radial stress which facilitates the formation of radial cracks [53]. By contract, higher compressive stress appeared in the TiN/g-TiSiN and TiN/g-TiSiN/TiSiN films, which inhibited the propagation of radial cracks to the surface of the film. Nest cracks, or inner circumferential cracks, which were parallel to the indenter edges at the coating surfaces can be observed inside the indented region of the two columnar-structured films [47,54], as marked by red arrows in Fig. 4a and b. Only a small number of nest cracks were observed near the indentation periphery of the impression of the TiN/g-TiSiN/TiSiN film shown in Fig. 4c, indicating the greatest contact damage resistance. No edge cracking was observed outside the contact periphery for all the tested samples.

It is important to note that a bright line was observed in the cross-sectional image from the indented TiN/g-TiSiN/TiSiN film, as marked by yellow arrows in Fig. 5c and d. This is speculated to be either a lateral or burst crack that occurred during nanoindentation or an artefact which was introduced during coating deposition. The same observation was found in TEM images recorded from the same sample (Fig. 7) as described in a later section of this paper.

TEM cross-sectional images

Bright field TEM images of the indents in the three films are shown in Figs. 6 and 7. These show the cross-sectional microstructure of these coatings in more detail. These cross-sectional TEM specimens, which

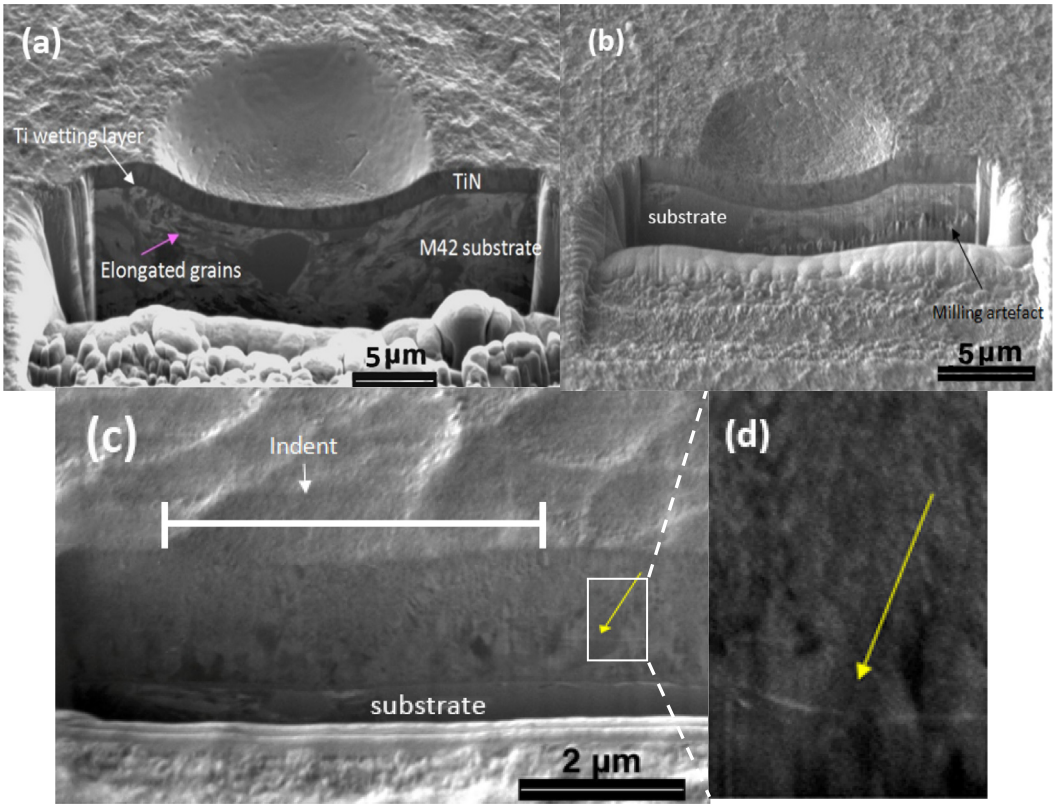

Fig. 5. FIB image of a cross-section of the indents of (a) TiN film, (b) TiN/g-TiSiN film and (c) TiN/g-TiSiN/TiSiN film following nanoindentation to a maximum load of 500 mN using a 5 µm radius spherical indenter. (d) A higher magnification image taken from marked region in (c).

were subjected to nanoindentation load of 500 mN using a 5 µm radius spherical indenter, were prepared across the center of the indents by a dual beam FIB (DB-FIB).

TiN and TiN/g-TiSiN films

Fig. 6a is a bright field TEM image recorded from the center of the indented region for the TiN film. A number of columnar cracks, marked by green arrows, are seen to extend from the bottom of the TiN film towards the top surface. It has been previously reported [51] that intercolumnar shear sliding was observed to be the dominant deformation mechanisms in indented TiN films. In addition, sliding or shearing of the columnar grains at grain boundaries results in shear steps near the interface between the coating and the substrate, as marked by white arrows. No delamination was found between the TiN coating and the substrate, even under the highest load of 500 mN, which indicates the good adhesion provided by the Ti wetting layer. Fig. 6b was recorded from the periphery of the spherically-indented region revealing a number of transverse microcracks, which appear to be almost near parallel to the undeformed coating surface, these are marked by pink arrows.

TEM cross-sectional images of the TiN/g-TiSiN film are shown in Fig. 6(c–e) for the entire coating, periphery and center of the indentation respectively. Four types of failure modes can be observed here, the columnar cracks (green arrows), fine transverse cracks (pink arrows), shear steps (white arrows), and radial cracks (purple arrows). When compared with the TiN film, the columnar cracks appear finer and can only be clearly seen in Fig. 6d. In addition, a small number of radial cracks are present at the bottom of the TiN layer close to the center of the indentation.

The observations suggest that radial cracks, rather than intercolumnar cracks, are the dominant fracture mechanism in the TiN/g-TiSiN film. Owing to the finer columnar structure, relative to the TiN film, the sliding of the columnar boundaries is restrained and a large tensile stress is distributed along the bottom of the TiN layer in the TiN/g-TiSiN film. Thus, the stress is released by means of radial cracking at the bottom of the TiN layer, which has lower mechanical strength than the TiSiN graded layer.

TiN/g-TiSiN/TiSiN film

The cracks present in the cross-sections of TiN/g-TiSiN/TiSiN film are different from the other two films because the residual indentation is shallower. A relatively small amount of plastic deformation occurs in both the substrate and the film. Fewer small intergranular cracks can be seen in the TiN layer, indicating that little of the shear stress is transmitted below the TiSiN nanocomposite layer that might cause slipping of columnar crystals along the grain boundaries. No obvious shear steps or radial cracks can be seen, which indicates the presence of a lower stress at the bottom of the film.

A small number of lateral cracks were observed clearly in the TiSiN nanocomposite layer, marked by yellow arrows. These cracks traverse the refined columnar grain structure and propagate from the center of the indentation to the outside and are parallel to the deformed film surface. At one side, near the center of the indentation, the crack started to bend toward the direction of the indentation axis. Also, there is a small amount of crack branching apparent in this part of the crack.

This observation agrees with the results reported by Ma et al. [10] who demonstrated that lateral cracking occurred more frequently in dual-layer films compared with binary films. The generation of lateral cracks may arise from a variety of factors [55–57]. First, is that the TiSiN nanocomposite layer is more brittle than the lower layers. The brittle layer releases stress through the formation of cracks rather than plastic deformation [55]. Second is the distinct microstructure between the TiSiN nanocomposite layer and the TiSiN graded layer. The cracks are generated readily in the transition region between these two layers due to the decrease of the shear stress applied on the oblique boundaries between the columnar grains during the transmission of the

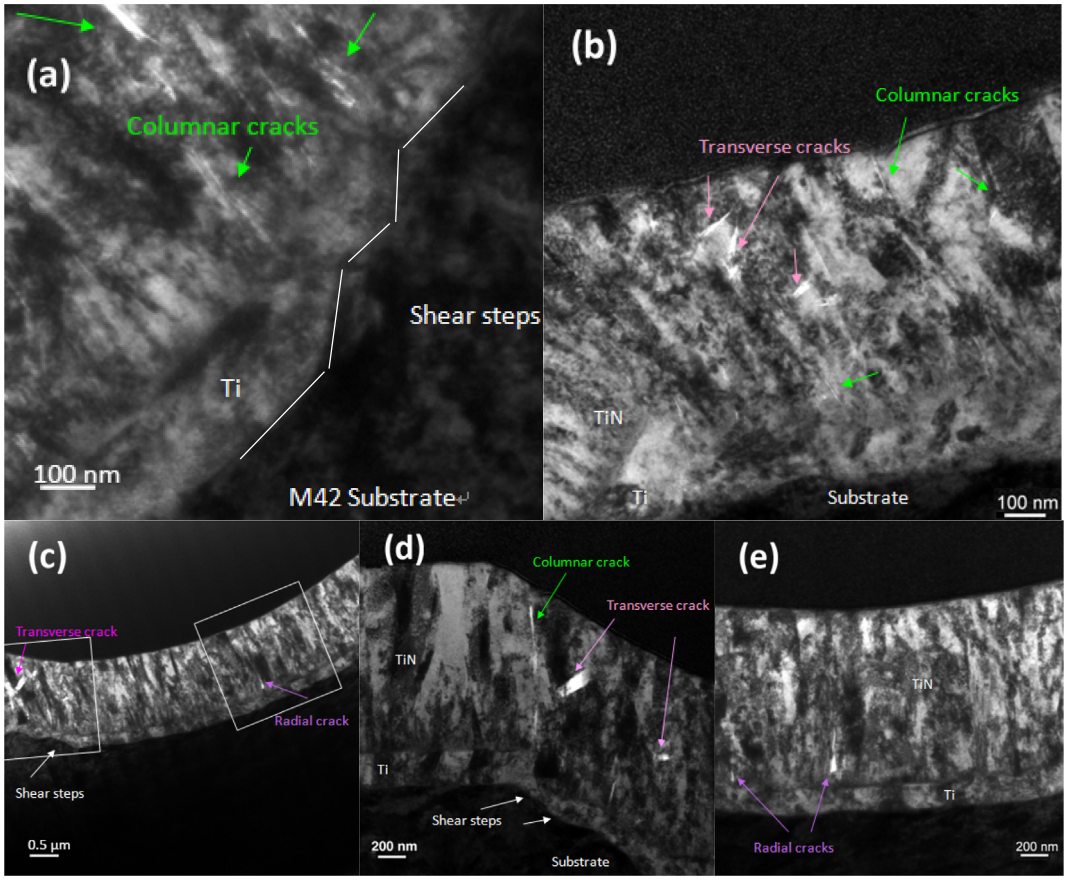

Fig. 6. (a) and (b) are bright field TEM images of the indents of the TiN film, following nanoindentation to a maximum load of 500 mN using a 5 μm radius spherical indenter. (a) is an image taken from the center of the indent and (b) is taken from the edge of the indent at high magnification. (c) is the bright field TEM images of TiN/g-TiSiN film, following nanoindentation to a maximum load of 500 mN using a 5 μm radius spherical indenter. (d) is a higher magnification image taken from the square left-hand side box in (c) and (e) is taken from the right-hand side square box in (c).

applied load. Third, with the incorporation of Si, the columnar grains become finer and are separated by amorphous Si_3N_4 along the growth direction. The resistant to the initiation of lateral cracks is reduced by the weakening of the orientation of grains.

According to the nanoindentation load–displacement curves. The initiation of lateral cracks in TiN/g-TiSiN/TiSiN film is related to the shear stress generated during the loading process, corresponding to the slight changes in the slope of the curve during loading. Conversely, the lateral crack will not be significantly deformed if the initiation of the cracks occurs during the unloading process. The further propagation of the lateral cracks corresponds to the abrupt change of the curve during the unloading phase. It has been shown [58] that the axial stress in the film can be generated by both the loading and unloading processes. The vertical compressive stress is produced in the compressive region during loading and relaxed during unloading. From the recovery of the elastic strain, the strain outside the compressive region is transferred to the compressive region through the film and converted into a tensile stress. The tensile stress generated during the unloading process leads to the generation of lateral cracks initiated in the loading process [59].

In brief, the dominant deformation mechanism in the TiN film is through columnar cracking and shear stepping. The dominant deformation mechanism in the TiN/g-TiSiN film is cracking in the bottom of the TiN layer, which results in radial cracks. The dominant deformation mechanism in the TiN/g-TiSiN/TiSiN film is the initiation and propagation of lateral cracks in the TiSiN graded layer. Please note, that most of the microcracks displayed in the TEM images described exist over very fine scale lengths so not readily resolved in the FIB images.

Finite element analysis

The stress distributions in the TiN/g-TiSiN/TiSiN film during the nanoindentation test was studied via finite element modelling to analyses their influence on the initiation of cracks within the sandwich structure, as compared with the TiN film and TiN/g-TiSiN film. According to the structural layering of these films, three distinct coatings systems are used in the simulation. Details of these coating systems are given in Table 1. (a, b and c represent the TiN film, TiN/g-TiSiN film and TiN/g-TiSiN/TiSiN film, respectively.)

The metal substrate is treated as an isotropic elastic–plastic material, with stress–strain behavior following a bilinear relation, as shown in Fig. 9, and assuming kinematic work-hardening and a von Mises yield criterion. The films are assumed to deform in linear elastic mode with isotropic elastic properties. Whilst elastic anisotropy has been observed in the TiN layer of each film, simulations of films with different elastic modulus values in-plane and out-of-plane indicated that the effect of elastic anisotropy on coating deformation behavior was minimal compared with the influences of sliding stress and the properties of the substrate [58]. Correspondingly, the fine structure in the TiSiN graded layer and the nanocomposite structure consisted of nc-TiN embedded in amorphous phase matrix in the TiSiN nanocomposite layer exhibit less prominent anisotropy. Accordingly, isotropic elastic properties were assumed in each layer of the films throughout the present study.

The mechanical properties for the materials used in the simulations are given in Table 2 [28,58]. Note that with the content of Si increasing gradually the mechanical properties of the TiSiN graded layer would change correspondingly. This complicates the determination of the

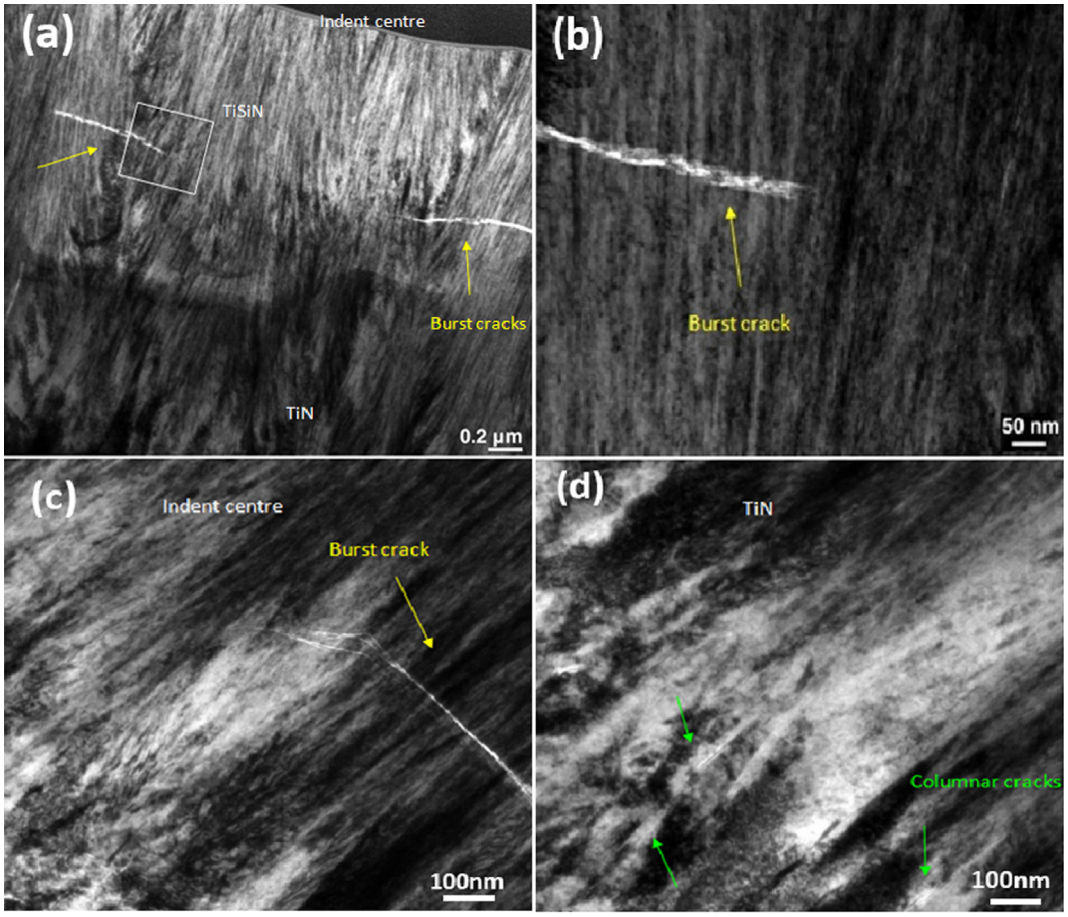

Fig. 7. Bright field TEM images of the indents in the TiN/g-TiSiN/TiSiN, following nanoindentation to a maximum load of 500 mN using a 5 μm radius spherical indenter. (a) BF TEM image taken from the center of the indent close to the surface. (b) is high-magnification BF-TEM image taken from the white square in (a). (c) is a high-magnification BF-TEM image taken from the other indent. (d) is a high-magnification BF TEM image of the TiN layer.

Table 2
The mechanical properties of materials involved in the modelling.

Parameters	Elastic modulus E (GPa)	Poisson's ratio υ	Yield strength σ_y (MPa)	Hardening modulus E_H (GPa)
TiSiN	600	0.20		
TiN	370	0.25		
Substrate (High-speed steel)	200	0.30	900	5
Si contents (at%)				
0	399.86	0.25		
2.08	417.03	0.25		
4.17	434.31	0.24		
6.25	470.23	0.23		
8.33	563.72	0.21		

mechanical properties of the TiSiN graded layer from the experiment. Thus, a first-principle theoretical calculation was performed to investigate the effect of Si additions on the mechanical properties of TiSiN. The calculated value of elastic modulus and Poisson's ratio were summarized in Table 2 and their function with Si concentration was shown in Fig. 8(a). The calculation indicated that the value of elastic modulus and Poisson's ratio can be approximately treated as linearly dependent on the Si content (from 0 to 10 at%). Comparing with the reported mechanical parameters [60–62], the calculation result had little difference with the experimental value and can be used as a set of parameters for mechanical properties of TiSiN graded layer.

In order to define the TiSiN graded layer in the finite element modelling and reflect the continuously changed composition in the TiSiN graded layer, two simplified assumptions were adopted in finite element simulation. The first was that the mechanical parameters of TiSiN graded layer was assumed to have a linear correlation with the Si concentration. As the fit curves shown in Fig. 8(a), the Poisson's ratio decreased linearly with the increase of Si concentration, while the elastic modulus observed an opposite trend. The second assumption is that the Si content would increase linearly with the film thickness in the TiSiN graded layer. To sum up, the distribution of elastic modulus and Poisson's ratio of the film/substrate system for the three samples was displayed in Fig. 8(b).

Fig. 9 shows the equivalent von Mises stress in the three films under a maximum load of 500 N applied by a spherical indenter. The indentation depths are shallow, except for the TiN thin film. The highest equivalent stress appears directly under the indenter within the film near the substrate for the TiN/g-TiSiN film. The stress here is tensile along the deformed spherical surface, which is the main reason for the formation of the radial cracks. The maximum equivalent stress in the TiN/g-TiSiN/TiSiN film appears in the TiN layer close to the interface with the TiSiN graded layer in the center of the indentation. which prevents the generation of columnar cracks, radial cracks and shear steps in the TiN layer. In Fig. 9 there is a relatively low stress concentration at the center of the indentation near the film surface and at the contact edge, which are locations where ring cracks and edge cracks are most likely to occur. There is also a small stress concentration region at the bottom of the film outside the indentation, which has been demonstrated by others to be associated with transverse shear stresses [28]. When this extends close to the interface, the transverse shear

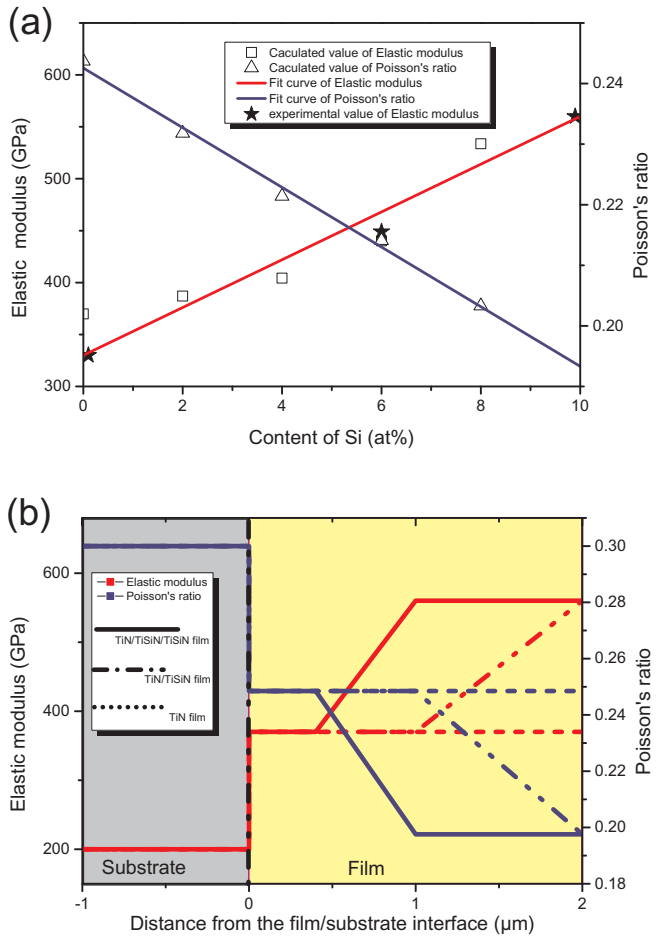

Fig. 8. (a) The calculated value of elastic modulus and Poisson's ratio with different concentrations of Si; (b) Distribution of elastic modulus and Poisson's ratio on thickness for the TiN film, TiN/g-TiSiN film and TiN/g-TiSiN/TiSiN film used in FEM.

stresses may result in both the formation of ring cracks and tilting of radial cracks [63]. It is the transversal shear stresses generated on loading that provide the possibility for the generation of lateral cracks [64]. However, in the TiN layer, where deformation is dominated by intercolumnar cracking, such stresses can effectively inhibit the initiation and propagation of lateral cracks due to the presence of columnar grains with vertically aligned grain boundaries. The transverse stress concentration region is smaller in the TiN/g-TiSiN film, indicating that the TiSiN graded layer in TiN/g-TiSiN/TiSiN film can effectively reduce this stress. Although the transverse stress does not lead to cracking in the TiN layer during the loading process, it will result in the initiation of lateral cracks in the TiSiN nanocomposite layer, when the value of the stress exceeds the fracture strength of TiSiN.

In conclusion, the FEM of the TiN/g-TiSiN/TiSiN films show that the introduction of the TiSiN graded layer can effectively re-configure the stress distribution of the film/substrate system, reduce the stress concentration in the film and suppress the generation of the radial cracks and columnar cracks at the bottom of film. This modelling also demonstrates the advantage of this form of coating architecture in terms of deformation resistance.

Conclusions

TiN/g-TiSiN/TiSiN thin films were prepared using unbalanced magnetron sputtering. The cross-sections of these thin films before, and after, indentation was examined by FIB imaging and TEM analysis. The

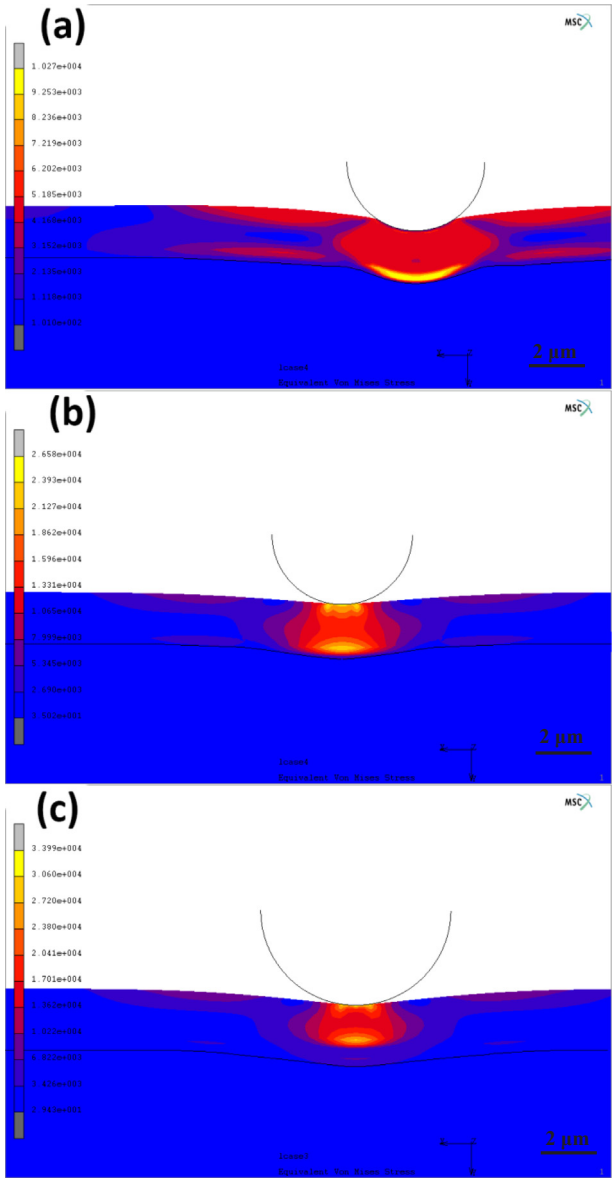

Fig. 9. Distribution of equivalent von Mises stress in the four coatings at the maximum indentation depth. (a) TiN film; (b) TiN/g-TiSiN film; (c) TiN/g-TiSiN/TiSiN film.

dominant deformation mechanisms in the TiN film, TiN/g-TiSiN film and TiN/g-TiSiN/TiSiN film were investigated and stress distributions in these thin films during indentation were analysis by FEM. The following conclusions can be drawn:

1. No delamination was observed in any the films when subjected to the maximum nanoindentation loads (500 mN).
2. The dominant deformation mechanism of the TiN film is the shear sliding of columnar grains along their boundaries, which resulted in a number intercolumnar cracks. The dominant deformation mechanism of the TiN/g-TiSiN film is the formation of radial cracks, which are the result of a tensile stress in the TiN layer. No sharp interface appeared with the gradual change of Si content. Further, the finer columnar structure in the TiN/g-TiSiN film led to smaller columnar cracks and stronger deformation resistance.
3. The TiN/g-TiSiN/TiSiN film showed the highest hardness and was more resistant to contact damage than the TiN film and TiN/g-TiSiN film. The TiSiN graded layer in the TiN/g-TiSiN/TiSiN film acted to modify the stress distribution and lower the stress concentration

level. The columnar structure in the TiSiN graded layer hindered lateral cracks from initiating and transferred the stress concentration from the TiN layer to the TiSiN nanocomposites layer. The lateral cracks in the TiSiN nanocomposites layer initiated on loading and continued to extend during unloading, which is seen as the dominant failure mode for the TiN/g-TiSiN/TiSiN film.

Acknowledgements

The authors acknowledge the financial support of the General Program of the National Natural Science Foundation of China under Grant No. 51675267, the Key Program of the National Natural Science Foundation of China under Grant No. 51635004 and the Australian Research Council Discovery Projects under Grant No. DP150102417.

References

[1] Zhang SY, Zhu WG. TiN coating of tool steels: a review. J Mater Process Technol 1993;39:165–77.
[2] Jeyachandran YL, Narayandass SK, Mangalaraj D, Areva S, Mielczarski JA. Properties of titanium nitride films prepared by direct current magnetron sputtering. Mater Sci Eng, A 2007;445-446:223–36.
[3] Chou WJ, Yu GP, Huang JH. Mechanical properties of TiN thin film coatings on 304 stainless steel substrates. Surf Coat Technol 2002;149:7–13.
[4] Penttinen IM, Korhonen AS, Harju E, Turkia MA, Forsén O, Ristolainen EO. Comparison of the corrosion resistance of TiN and (Ti, Al)N coatings. Surf Coat Technol 1992;50:161–8.
[5] Jeong YK, Kang MC, Kwon SH, Kim KH, Kim HG, Kim JS. Tool life of nanocomposite Ti-Al-Si-N coated end-mill by hybrid coating system in high speed machining of hardened AISI D2 steel. Curr Appl Phys 2009;9:S141–4.
[6] McIntyre D, Greene JE, Hakansson G, Sundgren JE, Munz WD. Oxidation of metastable single-phase polycrystalline Ti0.5Al0.5N films: kinetics and mechanisms. J Appl Phys 1990;67:1542–53.
[7] Uergen M, Cakir AF. The effect of heating on corrosion behavior of TiN- and CrN-coated steels. Surf Coat Technol 1997;96:236–44.
[8] Kumar CS, Patel SK. Performance analysis and comparative assessment of nanocomposite TiA1SiN/TiSiN/TiA1N coating in hard turning of AISI 52100 steel. Surf Coat Technol 2018;335:265–79.
[9] Abukhshim NA, Mativenga PT, Sheikh MA. Heat generation and temperature prediction in metal cutting: A review and implications for high speed machining. Int J Mach Tool Manufac 2006;46:782–800.
[10] Ma LW, Cairney JM, Hoffman MJ, Munroe PR. Deformation and fracture of TiN and TiAlN coatings on a steel substrate during nanoindentation. Surf Coat Technol 2006;200:3518–26.
[11] Yu XJ, Lai QX, Li GY, Xu JH, Gu MY. Mechanical properties and wear resistance of TaN/NbN nano-multilayers. J Mater Sci Lett 2002;21:1671–3.
[12] Veprek S. The search for novel, superhard materials. J Vac Sci Technol, A 1999;17:2401–20.
[13] Veprek S, Reiprich S, Li S. Superhard nanocrystalline composite materials: the TiN/Si3N4 system. Appl Phys Lett 1995;66:2640–2.
[14] Vepřek S, Reiprich S. A concept for the design of novel superhard coatings. Thin Solid Films 1995;268:64–71.
[15] Tang FZ, Gault B, Ringer SP, Cairney JM. Optimization of pulsed laser atom probe (PLAP) for the analysis of nanocomposite Ti-Si-N films. Ultramicroscopy 2010;110:836–43.
[16] Tang FZ, Gault B, Ringer SP, Martin P, Bendavid A, Cairney JM. Microstructural investigation of Ti-Si-N hard coatings. Scr Mater 2010;63:192–5.
[17] Prilliman SG, Clark SM, Alivisatos AP, Karvankova P, Vepřek S. Strain and deformation in ultra-hard nanocomposites nc-TiN/a-BN under hydrostatic pressure. Mater Sci Eng, A 2006;437:379–87.
[18] Veprek S, Veprek-Heijman MGJ, Karvankova P, Prochazka J. Different approaches to superhard coatings and nanocomposites. Thin Solid Films 2005;476:1–29.
[19] Diserens M, Patscheider J, Lévy F. Mechanical properties and oxidation resistance of nanocomposite TiN–SiNx physical-vapor-deposited thin films. Surf Coat Technol 1999;120–121:158–65.
[20] Ma LW, Cairney JM, Hoffman M, Munroe PR. Deformation mechanisms operating during nanoindentation of TiN coatings on steel substrates. Surf Coat Technol 2005;192:11–8.
[21] Cairney JM, Hoffman MJ, Munroe PR, Martin PJ, Bendavid A. Deformation and fracture of Ti–Si–N nanocomposite films. Thin Solid Films 2005;479:193–200.
[22] Meng WJ, Zhang XD, Shi B, Jiang JC, Rehn LE, Baldo PM, et al. Structure and mechanical properties of Ti–Si–N ceramic nanocomposite coatings. Surf Coat Technol 2003;163–164:251–9.
[23] Kim KH, Choi S-r, Yoon S-y. Superhard Ti–Si–N coatings by a hybrid system of arc ion plating and sputtering techniques. Surf Coat Technol 2002;161:243–8.
[24] Damadam M, Shao S, Ayoub G, Zbib HM. Recent advances in modeling of interfaces and mechanical behavior of multilayer metallic/ceramic composites. J Mater Sci 2018;53:5604–17.
[25] Saizonou C, Kouitat-Njiwa R, von Stebut J. Surface engineering with functionally graded coatings: a numerical study based on the boundary element method. Surf Coat Technol 2002;153:290–7.
[26] PalDey S, Deevi SC. Properties of single layer and gradient (Ti, Al)N coatings. Mater Sci Eng, A 2003;361:1–8.
[27] Suresh S, Olsson M, Giannakopoulos AE, Padture NP, Jitcharoen J. Engineering the resistance to sliding-contact damage through controlled gradients in elastic properties at contact surfaces. Acta Mater 1999;47:3915–26.
[28] Zhao X, Xie Z, Munroe P. Nanoindentation of hard multilayer coatings: Finite element modelling. Mater Sci Eng, A 2011;528:1111–6.
[29] Rowlands N, Munroe P. FIB for the evaluation of non-semiconductor materials. Materials Park: Asm International; 1999.
[30] Munroe PR. The application of focused ion beam microscopy in the material sciences. Mater Charact 2009;60:2–13.
[31] Perdew JP, Burke K, Ernzerhof M. Generalized gradient approximation made simple. Phys Rev Lett 1996;77:3865–8.
[32] Monkhorst HJ, Pack JD. Special points for Brillouin-zone integrations. Phys Rev B, Solid State (USA) 1976;13:5188–92.
[33] Zhang M, Lu MC, Du YH, Gao LL, Lu C, Liu HY. Hardness of FeB4: Density functional theory investigation. J Chem Phys 2014;140:6.
[34] Cairney JM, Harris SG, Munroe PR, Doyle ED. Transmission electron microscopy of TiN and TiAlN thin films using specimens prepared by focused ion beam milling. Surf Coat Technol 2004;183:239–46.
[35] Eriksson AO, Tengstrand O, Lu J, Jensen J, Eklund P, Rosen J, et al. Si incorporation in Ti1-xSixN films grown on TiN(001) and (001)-faceted TiN(111) columns. Surf Coat Technol 2014;257:121–8.
[36] Vaz F, Rebouta L, Almeida B, Goudeau P, Pacaud J, Rivière JP. Bessa e Sousa J, Structural analysis of Ti1 − xSixNy nanocomposite films prepared by reactive magnetron sputtering. Surf Coat Technol 1999;120–121:166–72.
[37] Soderberg H, Oden M, Larsson T, Hultman L, Molina-Aldareguia JM. Epitaxial stabilization of cubic-SiNx in TiN/SiNx multilayers. Appl Phys Lett 2006;88:3.
[38] Xiaoping H, Huijuan Z, Jiawei D, Geyang L, Mingyuan G. Study on the superhardness mechanism of Ti-Si-N nanocomposite films: influence of the thickness of the Si3N4 interfacial phase. J Vac Sci Technol, A 2005;23:114–7.
[39] Larsson M, Bromark M, Hedenqvist P, Hogmark S. Deposition and mechanical properties of multilayered PVD Ti − TiN coatings. Surf Coat Technol 1995;76–77:202–5.
[40] Sun SY, Liu XJ, Tan X, Jia HL, Tan XF. Off-Lattice KMC Simulation of the Growth Process of Ti-Si-N Film. In: Yuan L, editor. Mems, Nano and Smart Systems, Pts 1–6. Durnten-Zurich: Trans Tech Publications Ltd; 2012. p. 3636–41.
[41] Veprek S, Veprek-Heijman MGJ. The formation and role of interfaces in superhard nc-MenN/a-Si3N4 nanocomposites. Surf Coat Technol 2007;201:6064–70.
[42] Hultman L, Bareño J, Flink A, Söderberg H, Larsson K, Petrova V, et al. Interface structure in superhard TiN-SiN nanolaminates and nanocomposites: film growth experiments andab initiocalculations. Phys Rev B 2007;75.
[43] Wo PC, Munroe PR, Zhou ZF, Li KY, Xie ZH. Effects of TiN sublayers on the response of TiSiN nanocomposite coatings to nanoidentation and scratching contacts. Mater. Sci. Eng., A 2010;527:4447–57.
[44] Weppelmann ER, Hu XZ, Swain M. Observation and simple fracture mechanics analysis of indentation fracture delamination of TiN films on silicon. J Adhes Sci Technol 1994;8(6):611–24.
[45] Hainsworth SV, Bartlett T, Page TF. The nanoindentation response of systems with thin hard carbon coatings. Thin Solid Films 1993;236:214–8.
[46] Rabe R, Breguet JM, Schwaller P, Stauss S, Haug FJ, Patscheider J, et al. Observation of fracture and plastic deformation during indentation and scratching inside the scanning electron microscope. Thin Solid Films 2004;469–470:206–13.
[47] Richter J. Application of Vickers indentation for assessment of PVD TiN coated new nonledeburitic high-speed steels. Surf Coat Technol 2003;162:119–30.
[48] Ma LW, Cairney JM, Hoffman MJ, Munroe PR. Characterization of TiN thin films subjected to nanoindentation using focused ion beam milling. Appl Surf Sci 2004;237:631–5.
[49] Bhowmick S, Bhide R, Hoffman M, Jayaram V, Biswas SK. Fracture mode transitions during indentation of columnar TiN coatings on metal. Phil Mag 2005;85:2927–45.
[50] Fischer-Cripps AC, Lawn BR, Pajares A, Lanhua W. Stress analysis of elastic-plastic contact damage in ceramic coatings on metal substrates. J Am Ceram Soc 1996;79:2619–25.
[51] Ma LW, Cairney JM, Hoffman MJ, Munroe PR. Effect of coating thickness on the deformation mechanisms in PVD TiN-coated steel. Surf Coat Technol 2010;204:1764–73.
[52] Abdul-Baqi A, Van der Giessen E. Numerical analysis of indentation-induced cracking of brittle coatings on ductile substrates. Int J Solids Struct 2002;39:1427–42.
[53] Singh RK, Zhou Z, Li LKY, Munroe P, Hoffman M, Xie Z. Design of functionally graded carbon coatings against contact damage. Thin Solid Films 2010;518:5769–76.
[54] Ma KJ, Bloyce A, Bell T. Examination of mechanical properties and failure mechanisms of TiN and Ti − TiN multilayer coatings. Surf Coat Technol 1995;76–77:297–302.
[55] Swain MV. Microfracture about scratches in brittle solids. Proc R Soc Lond A, Math Phys Sci (UK) 1979;366:575–97.
[56] Ahn Y, Farris TN, Chandrasekar S. Sliding microindentation fracture of brittle materials: Role of elastic stress fields. Mech Mater 1998;29:143–52.
[57] Jing X, Maiti S, Subhash G. A new analytical model for estimation of scratch-induced damage in brittle solids. J Am Ceram Soc 2007;90:885–92.
[58] Tilbrook MT, Paton DJ, Xie Z, Hoffman M. Microstructural effects on indentation failure mechanisms in TiN coatings: finite element simulations. Acta Mater 2007;55:2489–501.
[59] Abdul-Baqi A, Van der Giessen E. Delamination of a strong film from a ductile

substrate during indentation unloading. J Mater Res 2011;16:1396–407.
[60] Li W, Liu P, Zhu XD, Zhang K, Ma FC, Liu XK, et al. Influence of TiN-nanolayered insertions on microstructure and mechanical properties of TiSiN nanocomposite film. J Mater Sci 2014;49:4127–32.
[61] Zhang T, Huan Y. Nanoindentation and nanoscratch measurements on submicron TiN coatings. Acta Mech Sin (China) 2003;35:498–502.
[62] Cheng YH, Browne T, Heckerman B. Nanocomposite TiSiN coatings deposited by large area filtered arc deposition. J Vac Sci Technol, A 2009;27:82–8.
[63] Singh RK, Tilbrook MT, Xie ZH, Bendavid A, Martin PJ, Munroe P, et al. Contact damage evolution in diamondlike carbon coatings on ductile substrates. J Mater Res 2011;23:27–36.
[64] Abdul-Baqi A, Van der Giessen E. Indentation-induced interface delamination of a strong film on a ductile substrate. Thin Solid Films 2001;381:143–54.